JOURNAL OF PROPULSION AND POWER
Vol. 30, No. 1, January–February 2014

Damping Coefficient Prediction of Solid Rocket Motor Nozzle Using Computational Fluid Dynamics

Afroz Javed* and Debasis Chakraborty†
Defence Research and Development Laboratory, Hyderabad 500058, India

DOI: 10.2514/1.B35010

Numerical simulations are carried out to evaluate the nozzle damping of rocket motors. A subscale cold flow experimental condition where nozzle damping coefficients are evaluated through the pulse decay method is taken as a validation case. The flowfield of the motor is simulated by solving three-dimensional Reynolds-averaged Navier–Stokes equations using commercial computational fluid dynamics software. The trend of the pressure decay in the head end is well captured for different values of port-to-throat area ratios, and a very good match is obtained between the computed and experimental values of the nozzle decay coefficient. Validated methodology is used to evaluate the damping coefficient of a burning solid rocket motor with composite propellant.

I. Introduction

THE susceptibility of solid-propellant rocket motors to combustion instability depends upon the nature of the interactions between the flow disturbances and the various processes taking place inside the combustor and the nozzle. Some of these interactions, such as the one with the combustion process, tend to increase the energy of the flow disturbances and thus exert a destabilizing influence upon the motor. Other interactions, such as those with the wave motion in the nozzle, with aluminum oxide particles in the combustor, and so on, tend to dissipate the energy of the flow disturbances and thus exert a stabilizing influence upon the motor. Thus, performing a meaningful stability analysis of a solid-propellant rocket motor calls for an evaluation of the energy balance between the various disturbance (or wave) energy gains and disturbance energy losses that pertain to the motor under consideration. The principle damping mechanisms in a solid motor are nozzle damping, particle damping, mean flow/acoustic interactions, and structural damping. Nozzle damping is usually the largest damping mechanism in a motor, particularly with longitudinal and mixed transverse/longitudinal modes [1]. In the past, several experimental and analytical studies have been carried out for the evaluation of nozzle damping. Most of the experimental studies [2–5] have been carried out simulating a solid rocket motor flowfield with a cold flow test. In these cold flow tests, air is used as the fluid in the simulated motor at normal temperatures. Analytical models for the evaluation of the nozzle damping coefficient have been suggested by Zinn [6] considering short nozzle approximation, that is, nozzle convergent length to be smaller than the wavelength of the first mode of longitudinal oscillations. Dehority [7] further suggested some modifications for the analytical estimation of the nozzle damping coefficient. The flow through a nozzle of a solid-propellant rocket motor is choked, which results in the nozzle losses being represented as a function of the specific heat of the gas and the Mach number at the nozzle entrance. This loss occurs because some of the acoustic wave is reflected back into the motor, while a large portion of the wave travels through the nozzle and exits the motor, reducing the total acoustic energy. This effect is highest when the mean flow velocity at the nozzle entrance is at a maximum, resulting in the nozzle damping being at a maximum at the initial stage of the burn time because the port area is small and the resulting mean flow velocity is high. The nozzle damping decreases as the mean flow velocity decreases with the increasing port. This variation in the nozzle damping makes it necessary to estimate the damping characteristics at different stages of grain burning.

In the present work, computational fluid dynamics (CFD) techniques are used to evaluate the damping caused due to the nozzle by solving three-dimensional Navier–Stokes equations. An experimental case reported in the literature by Buffum et al. [2], where subscale tests have been carried out to evaluate the nozzle damping coefficient, is considered for the validation test for the computational model. In the experimental study, three methods, namely, pulse decay, steady-state decay, and steady-state resonance, have been used. In the present study, the pulse decay method has been considered because it is computationally least expensive among all the three methods in terms of time required to carry out the simulations.

II. Details of Geometry and Numerical Simulation

A schematic of the geometry considered for simulations taken from Buffum et al. [2] is shown in Fig. 1. The length L of the cylindrical port and throat diameter D_t are kept constant with the values of 0.30 and 0.0064 m, respectively. The port diameter D_p is varied to achieve different values of throat-to-port diameter ratios J. Table 1 shows the different values of port diameters considered and resulting throat-to-port diameter ratios.

A steady flow of air is provided from the side walls of the motor in the radial direction, at a pressure of 2.4 bar and 300 K. This flow is exhausted through the convergent–divergent nozzle. The length of the nozzle convergent portion is around 0.006 m, which can be easily neglected in comparison with the length of tube (0.30 m). The fundamental acoustic frequency of the tube would be around 570 Hz, with the acoustic speed at 300 K, and length of the tube as half wavelength. The time period of the standing wave would be around 1753 μs.

A 10 deg sector of the geometry is considered for numerical simulations due to the symmetry of the geometry. CFX Build software has been used to generate hexahedral grids. The grids are clustered toward the injecting side and nozzle walls to capture the flow gradients. Fine uniform mesh is used in the axial direction. Figure 2 shows a picture of the grids, with zoomed views at the head and nozzle ends. A grid convergence study is carried out by considering 0.12 and 0.26 million grids for the validation case. Simulations are carried out for laminar and turbulent flows considering the k-ε turbulence model. The pressure at the centerline is monitored for all the simulations and is shown in Fig. 3 in much zoomed scale. It can be observed that the turbulent simulations give marginally higher (0.5%) head end pressure compared with laminar simulations. The differences between the pressures from the two

Received 4 April 2013; revision received 11 July 2013; accepted for publication 29 July 2013; published online 31 December 2013.

*Scientist; ajaved@drdl.drdo.in.
†debasis_cfd@drdl.drdo.in.

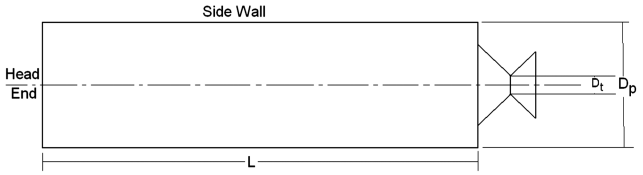

Fig. 1 Schematic geometry for the cold flow rocket motor simulations [2].

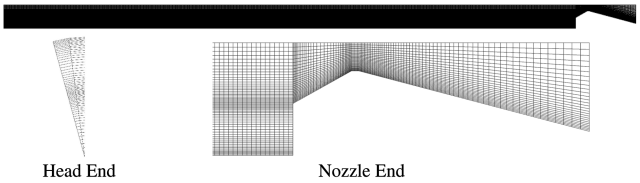

Fig. 2 Typical grids for cold flow rocket motor simulations showing zoomed view of grid at head and nozzle ends.

grids are negligible. Based on these observations, 0.12 million grid points are considered for further simulations.

CFX11 commercial CFD solver [8] software has been used for the transient simulations of the flowfield. This software is capable of solving the Navier–Stokes equations using the finite volume method for both laminar and turbulent flow conditions. For the present simulations, a second-order scheme for both temporal and spatial discretization is selected for solving Reynolds-averaged Navier–Stokes equations. A laminar flowfield is considered inside the tube because turbulence is found to have a negligible effect on the flowfield, as shown in Fig. 3. The effect of turbulence on the wave motion is also observed to be small, as will be explained later.

The required mass flow rate of the air to achieve the chamber pressure of 2.4 bar is given as a source term from the side walls of the motor. In the experiments carried out by Buffum et al. [2], the pulse decay test has been carried out by giving a pulse of pressure from the bursting of a diaphragm. This pulse has been found to be around 0.35 bar above the mean pressure. The chamber pressure is monitored at the head end of the motor. Once the chamber pressure reaches a constant value and the flowfield is well established in the motor, a sinusoidal pressure pulse is applied at the head end with an amplitude of 0.35 bar relative to the mean pressure. After one wavelength of applied pressure pulse, which takes a time period of around 877 μs, it is removed, and the pressure is monitored at the head end. A similar exercise is carried out for rest of the five geometries and the decay of the pressure pulse is analyzed at the head end for the evaluation of the nozzle damping coefficient.

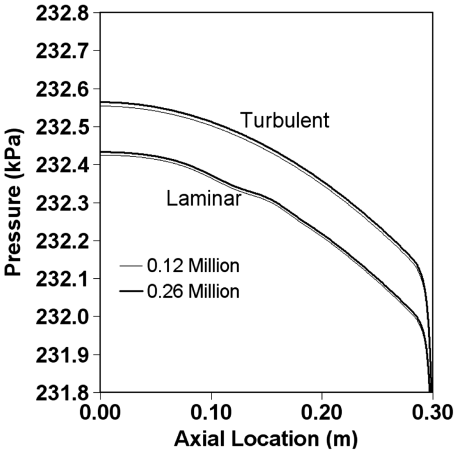

Fig. 3 Static pressure at the centerline for two different grids with turbulent and laminar simulations.

III. Results and Discussion

A part of the pressure pulse applied from the head end gets reflected from the nozzle end and the rest is transmitted to the atmosphere through the nozzle exit. With further reflections from both the head and nozzle ends, the amplitude keeps on reducing. The head end pressure variations for different J value cases are shown in Fig. 4. Examination of this figure shows a nonsinusoidal behavior, as was observed by Buffum et al. [2], resulting in a multimode damping phenomenon. Further inspection of Fig. 4 reveals that the pressure fluctuations are damped sharply for a smaller port area, as expected from the reported experimental and analytical studies. It can also be observed that some more frequencies get excited at higher port areas other than the fundamental mode. A similar kind of behavior is observed in the experimental and analytical analyses carried out by Nasr et al. [9].

The monitored pressure at the head end can be represented in the form of $p(t) = p_0 \sin(2\pi f.t) \times e^{-\alpha t}$, where p_0 is the initial amplitude, f represents the natural frequency, and α is defined as the nozzle damping coefficient. The value of the nozzle damping coefficient can be evaluated as

$$\alpha = \frac{1}{t_2 - t_1} \ln\left(\frac{p_1}{p_2}\right)$$

Table 1 Port diameters considered for numerical simulations

Case no.	1	2	3	4	5	6
D_p, m	0.025	0.038	0.051	0.064	0.076	0.089
J	0.0625	0.0278	0.0156	0.0100	0.0069	0.0051

where p_1 and p_2 are the values of two consecutive pressure peaks or valleys and t_1 and t_2 are the respective time instants. The nozzle damping coefficient is evaluated for all the six cases. It is found to be highest for the smallest port diameter and decreases with the increase in port diameter with the smallest for the largest port diameter. This trend is found to be in accordance with earlier theoretical and experimental observations. When these values are compared with the reported experimental values, it has been observed that a good match exists between the experimentally evaluated nozzle damping coefficient and those evaluated using the CFD technique, as shown in Table 2.

It can also be observed from Table 2 that, with the decrease in the value of J, the nozzle damping coefficient also decreases. It indicates that, during the operation of a solid rocket motor, the nozzle damping is at maximum at its start due to lowest port area and, as the burning proceeds and port area increases, the damping of pressure oscillations caused due to the nozzle decreases. Hence, the motors are more susceptible to instability at the later part of their operation than in the beginning. A higher nozzle damping coefficient would always be desirable from the stability point of view. CFD techniques can be very useful in designing a rocket motor with a reliable evaluation of the nozzle damping coefficient.

IV. Simulation for a Composite-Propellant Rocket Motor

The validated methodology is applied to predict the nozzle damping coefficient of a solid rocket motor with composite propellant. Three different geometries corresponding to the initial time, 2, and 4 s burn time are studied for the evaluation of nozzle damping coefficients at these instants. The typical grain geometry of the rocket motor is shown in Fig. 5, which has a finocyl shape at the nozzle end. The symmetry of the geometry allows for the simulation of a 45 deg sector. Unstructured tetrahedral grids are made using ICEM CFD [10] software. Fine hexahedral grids are used near the grain surfaces and nozzle walls to capture the gradients occurring in these regions. A typical grid with zoomed views at different regions is shown in Fig. 6. The minimum resolution near the grain wall is kept at 0.1 mm. Grid convergence studies are carried out for a composite-propellant rocket motor by considering 0.74 and 1.42 million grids.

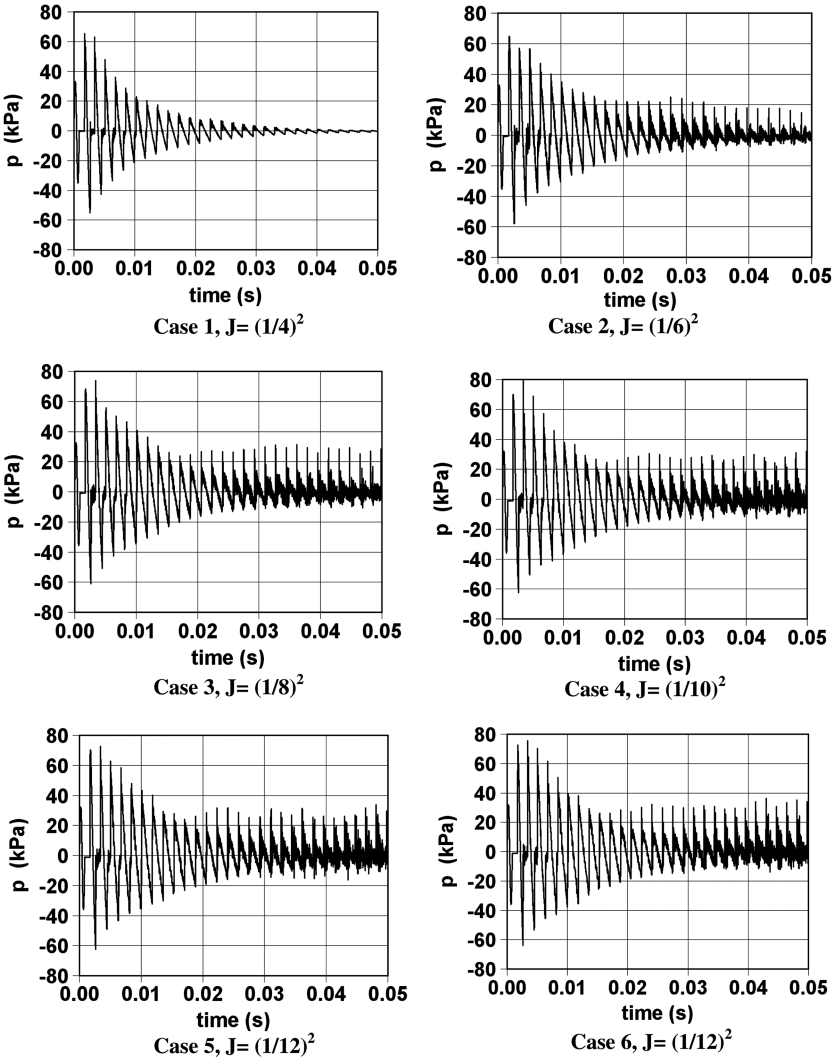

Fig. 4 Damping of the head end pressure signal for different cases.

Simulations are also carried out for laminar and turbulent (k-ε turbulence model) conditions. Figure 7 depicts the pressure at the centerline for all the simulations. Here also, turbulent simulations show marginal difference (0.8% more) in the head end pressure compared with laminar simulations. The pressure distributions between two grids coincide, demonstrating the grid independence of the results. Based on these observations, 0.74 million grid points are considered for further simulations.

The flow simulations are carried out using the CFX11 commercial CFD solver [8]. For the present simulations, the grain surface is set as the inlet with the propellant mass flow rate applied as the boundary condition. Two sides are taken as symmetry boundary conditions and the nozzle wall and head end wall are taken as no-slip adiabatic walls. A supersonic outflow boundary condition is prescribed at the outlet because the flow at the nozzle exit is supersonic. The locations of different boundaries are shown in Fig. 8. A laminar flowfield is considered inside the motor because turbulence is found to have a negligible effect on flowfield, as shown in Figs. 3 and 7. The effect of turbulence on the wave motion is also investigated and the results are shown in Fig. 9. The pressures are monitored at the head end for both laminar and turbulent simulations. Laminar and turbulent solutions superimpose on each other. To observe a difference, one of the peaks is zoomed several times to show two different lines for laminar and turbulent simulation results. Hence, simulations with laminar flowfields are considered adequate for flow explorations.

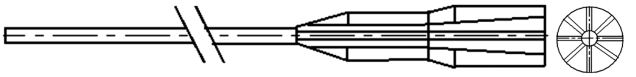

Fig. 5 Schematic grain geometry.

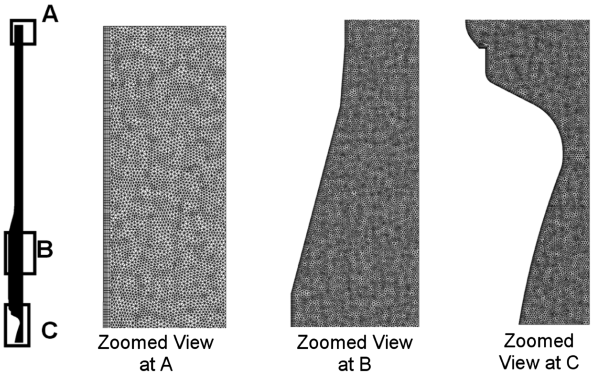

Fig. 6 Computational grid for the motor geometry.

Table 2 Experimental and calculated values of nozzle damping coefficient

Case no.	1	2	3	4	5	6
J	0.0625	0.0278	0.0156	0.0100	0.0069	0.0051
α experimental, s^{-1}	—	160	114	82	71	48
α calculated, s^{-1}	173	148	103	80	69	47

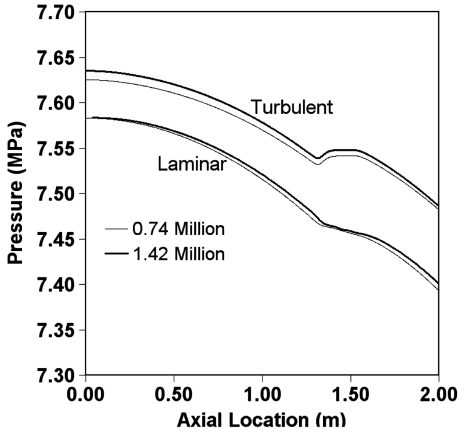

Fig. 7 Static pressure at the centerline for two different grids with turbulent and laminar simulations.

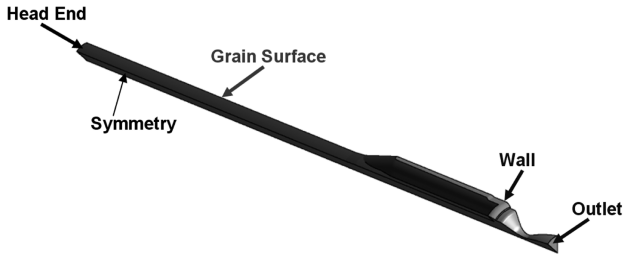

Fig. 8 Motor geometry for the simulation with the boundary locations.

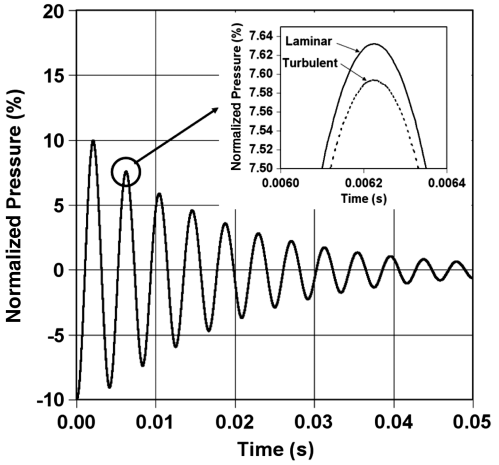

Fig. 9 Damping of the pressure signal with laminar and turbulent flowfields.

The thermochemical properties of the combustion gases used for the simulations are given in Table 3. Thermochemical properties are obtained from the NASA CEA 600 [11,12] program for equilibrium calculations for the given propellant combination. With these properties, the acoustic speed in the combustion chamber would be 1074.3 m/s.

Table 3 Thermochemical properties of the combustion gases

Property	Value
Total temperature	2980 K
Ratio of specific heats	1.214
Molecular weight	25.1
Thermal conductivity	0.4058 W/m · K
Dynamic viscosity	9.513×10^{-5} Pa · s

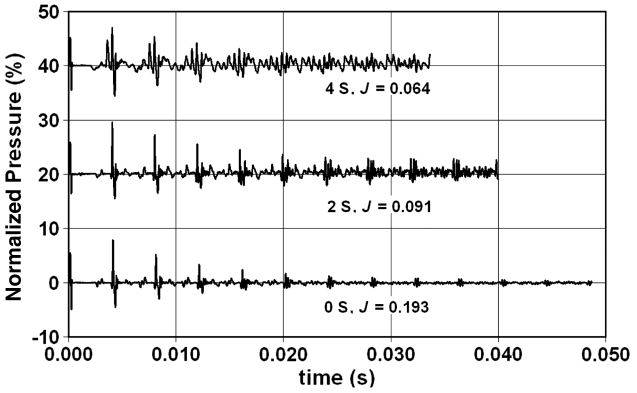

Fig. 10 Damping of the head end pressure signal for motor burning cases.

Second-order numerical schemes for both spatial and temporal resolution are used. A physical time step of 5 μs is used for the unsteady simulations. Before running the unsteady simulations, a steady-state solution has been obtained. This steady-state flowfield is taken as the initial condition for the unsteady simulation. A pressure pulse is given in the form of a sine wave with a peak value of around 8–10% of the mean pressure. The time period of this pressure pulse is 100 μs, after which it is removed. The pressure field at the head end is monitored, after giving a pressure pulse from the head end. The normalized temporal pressures at the head end with geometries at different time instants are shown in Fig 10. In this figure, the result for each geometry is translated by 20% in the y direction. It can be clearly observed that the pressure perturbation for the initial geometry ($t = 0$ s) damps quickly compared with the cases for higher port areas at $t = 2$ and 4 s. The excitation of other subharmonics can also be observed in Fig. 10 for lower values of J. The nozzle damping coefficients for different geometries at three different time instants are presented in Table 4.

The computed nozzle damping coefficient shows a decrease in value with increasing port area or decreasing J value, as shown in Table 4. With the finocyl shape of the motor grain, after the web burn, there is only a small increase in the port area with time and, consequently, the nozzle damping coefficient shows its maximum value at the beginning and becomes nearly constant at a lower value after the web is burned out.

It can be observed from Fig. 10 that the pressure signal shows a wave packet kind of signature. To find the effect of this signature on nozzle damping, simulations are carried out with a sinusoidal disturbance to evaluate the damping coefficient. A pressure disturbance in the form of a half-sine wave with the fundamental longitudinal frequency of the rocket motor was given along the length of the motor with an amplitude of 10% of the head end pressure. Decay of this pressure signal on the head end is monitored with time. The results of these simulations are shown in Fig. 11. In this figure, the result for each geometry is translated by 30% in the y direction. The calculated values of nozzle damping coefficients are shown in Table 4. A comparison of the damping coefficient evaluated using a pulse of disturbance at the head end and those evaluated using a sinusoidal wave of fundamental frequency shows that the damping coefficients for nonfundamental frequency cases are higher than those observed for sinusoidal cases with a fundamental frequency. This happens due to the multimode damping occurring in the previous case. This difference is experimentally observed by Buffum et al. [2] also, where they have evaluated damping coefficients using

Table 4 Calculated values of nozzle damping coefficient

Time instant	0 s	2 s	4 s
J	0.193	0.091	0.064
α calculated, s^{-1} (pulse)	113	70	67
α calculated, s^{-1} (sinusoidal signal with fundamental frequency)	56	34	33

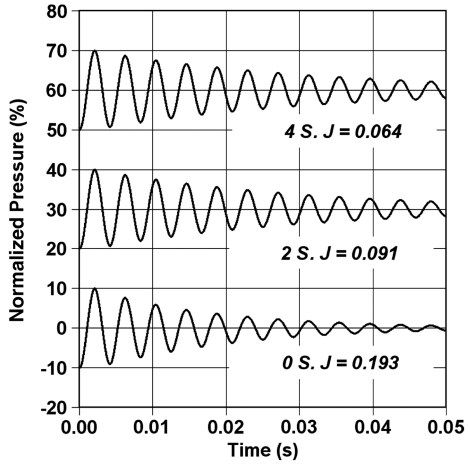

Fig. 11 Damping of sinusoidal head end pressure signal with fundamental frequency for motor burning cases.

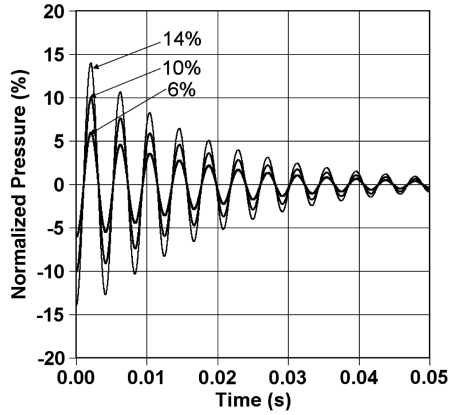

Fig. 12 Damping of pressure signal with different amplitudes.

steady-state resonance and steady-state decay techniques. In these techniques, the chamber is excited by a monochrome sinusoidal wave. The results for damping coefficients from these techniques were compared with those observed from the pulse decay technique. It is reported that the pulse decay technique shows a rapid fall in the pressure signal, resulting in a higher damping coefficient. Multimode damping due to the presence of several frequencies in the motor chamber is expected to be responsible for the higher nozzle damping coefficients.

The change of oscillation amplitudes is also studied for this motor by varying the initial pulse strength as 6, 10, and 14% of the head end pressures for the 0 s case. The oscillations with different amplitudes are shown in Fig. 12. The damping coefficient is evaluated for all three cases and found to be independent of the strength of the pressure pulse in the range considered.

V. Conclusions

CFD simulations are carried out for a cold flow experimental condition to estimate the nozzle damping coefficient. A pressure pulse is applied at the motor head end for one wavelength and the decay of pressure is observed with time. It is observed that the pressure decay is at its maximum for the highest throat-to-port area ratio J and reduces monotonically. The computed and experimental values of the nozzle damping coefficient show a good match. At lower values of J, excitation of other subharmonics are also observed, in accordance with similar observations reported in literature. The estimation of the nozzle damping coefficient for a solid rocket motor with a composite propellant also shows similar behavior.

References

[1] Blomshield, F. S., "Lessons Learned in Solid Rocket Combustion Instability," AIAA Paper 2007-5803, 2007.

[2] Buffum, F. G., Dehority, G. L., Slates, R. O., and Price, E. W., "Acoustic Attenuation Experiments on Subscale Cold-Flow Rocket Motors," *AIAA Journal*, Vol. 5, No. 2, 1967, pp. 272–280. doi:10.2514/3.3952

[3] Bell, W. A., Daniel, B. R., and Zinn, B. T., "Experimental and Theoretical Determination of the Admittances of a Family of Nozzles Subjected to Axial Instabilities," *Journal of Sound and Vibration*, Vol. 30, No. 2, 1973, pp. 179–190. doi:10.1016/S0022-460X(73)80112-9

[4] Janardan, B. A., Daniel, B. R., and Zinn, B. T., "Scaling of Rocket Nozzle Admittances," *AIAA Journal*, Vol. 13, No. 7, 1975, pp. 918–923. doi:10.2514/3.60470

[5] Culick, F. E. C., and Dehority, G. L., "Analysis of Axial Acoustic Waves in a Cold-Flow Rocket," *Journal of Spacecraft and Rockets*, Vol. 6, No. 5, 1969, pp. 591–595. doi:10.2514/3.29618

[6] Zinn, B. T., "Nozzle Damping in Solid Rocket Instabilities," *AIAA Journal*, Vol. 11, No. 11, 1973, pp. 1492–1497.

[7] Dehority, G. L., "Resume of Nozzle Damping Theory," Naval Weapons Center, TM-2867, China Lake, CA, 1976.

[8] "ANSYS CFX 11.0," Ver. 11.0, ANSYS, Canonsburg, PA, Jan. 2007.

[9] Nasr, M., Hegab, A. M., El-Askary, W. A., and Yousif, K. A., "Investigation on the Internal Flow in Simulated Solid Rocket Motor Chamber/Nozzle Configuration," *13th International Conference on Aerospace Sciences & Aviation Technology*, Paper ASAT-13-PP-12, Military Technical College, Cairo, Egypt, 26–28 May 2009.

[10] "ICEM CFD-11, Installation and Overview," ANSYS, Canonsburg, PA, Jan. 2007.

[11] Gordon, S., and McBride, B. J., "Computer Program for Calculation of Complex Chemical Equilibrium Compositions and Applications. I. Analysis," NASA RP-1311, 1994, p. 20.

[12] Gordon, S., and McBride, B. J., "Computer Program for Calculation of Complex Chemical Equilibrium Compositions and Applications. II. Users Manual and Program Description," NASA RP-1311, 1996, p. 73.

K. Frendi
Associate Editor